

# Metallic quantum criticality enabled by flat bands in a kagome lattice

Lei Chen<sup>1</sup>, Fang Xie<sup>1</sup>, Shouvik Sur<sup>1</sup>, Haoyu Hu<sup>2</sup>,  
Silke Paschen<sup>3,1</sup>, Jennifer Cano<sup>4,5</sup>, Qimiao Si<sup>1,\*</sup>

<sup>1</sup> *Department of Physics and Astronomy, Rice Center for Quantum Materials, Rice University, Houston, Texas, 77005, USA*

<sup>2</sup> *Donostia International Physics Center, P. Manuel de Lardizabal 4 20018 Donostia-San Sebastian, Spain*

<sup>3</sup> *Institute of Solid State Physics, Vienna University of Technology, Wiedner Hauptstr. 8-10, 1040 Vienna, Austria*

<sup>4</sup> *Department of Physics and Astronomy, Stony Brook University, Stony Brook, NY 11794, USA*

<sup>5</sup> *Center for Computational Quantum Physics, Flatiron Institute, New York, NY 10010, USA*

**Strange metals arise in a variety of platforms for strongly correlated electrons, ranging from the cuprates, heavy fermions to flat band systems. Motivated by recent experiments in kagome metals, we study a Hubbard model on a kagome lattice whose noninteracting limit contains flat bands. A Kondo lattice description is constructed, in which the degrees of freedom are exponentially localized molecular orbitals. We identify an orbital-selective Mott transition through an extended dynamical mean field theory of the effective model. The transition describes a quantum critical point at which quasiparticles are lost and strange metallicity emerges. Our theoretical work opens up a new route for realizing beyond-Landau quantum criticality and emergent quantum phases that it nucleates.**

\*To whom correspondence should be addressed; E-mail: qmsi@rice.edu.

## Introduction

In quantum materials, strong correlations give rise to a rich landscape of quantum phases [1, 2]. Microscopically, strong correlations arise when the partially-filled atomic orbitals near the Fermi energy make the electrons to experience a larger electrostatic repulsive interaction than their kinetic energy [3, 4, 5]. The advent of moiré systems has highlighted the notion of flat bands – bands of Bloch electron states that hardly disperse [6, 7]. Such flat bands are also being investigated in materials with kagome and other line-graph lattices [8, 9, 10, 11], where a destructive interference of electron motion leads to a reduction in the bandwidth and proportionally enhances the effect of electron interaction. These studies represent a part of extensive ongoing efforts on metals with kagome and related crystal structures. Most of the existing efforts have focused on static though unusual electronic orders such as charge density wave [12, 13, 14, 15, 16, 17].

A central theme of strongly correlated electrons is strange metallicity, which is signified by anomalous temperature and/or frequency dependences in their electrical transport, spin/charge dynamics and thermodynamic properties [18, 19, 20, 21]. Such metals are typically located at the border of localization, as implicated by a jump of the Fermi surface [22, 23, 24]; when they are associated with metallic quantum criticality, they implicate a type of quantum critical points that go beyond the Landau framework of order-parameter fluctuations [25, 26, 27]. Recently, strange metallicity has also been observed in metals of kagome and related line-graph crystalline structures [28, 29, 30], raising the question about its origin and, more generally, whether and how it is connected with the strange metallicity of more familiar platforms.

In kagome metals, the destructive interference of electron motion underlies flat bands on line-graph lattices. Electrons partially occupying a flat band are prone to developing quantum fluctuations that go beyond static ordering. To study such fluctuations, it is important to treat

the correlation effects of the flat bands in terms of variables that preserve the symmetry of the Hamiltonian. The flat bands can be visualized in terms of compact localized states in real space [31, 32]. Consider the case of a kagome metal, a two-dimensional lattice built up from corner-sharing triangles [Fig. 1(a)]. The wavefunction of the compact localized state, with its amplitude and phase illustrated in Fig. 1(b), suggests that the flat band could possibly be described by a molecular orbital. The challenge, however, is that the flat band is topological [33, 34]. The latter prevents a representation of the flat band alone in terms of exponentially localized and Kramers-doublet Wannier orbitals [35]. Indeed, the compact localized state illustrated in Fig. 1(b) is not a proper representation of the flat band: such local states from different sites do not form a complete orthonormal basis [31, 32].

Here we construct the proper molecular orbitals through a Wannierization procedure that resolves the topological obstruction. These tight molecular orbitals are represented by the most localized Wannier orbitals [see Fig. 2(b) and the Supplementary Materials (SM), Sec. C], which predominantly though not exclusively incorporate the flat bands and form a triangular lattice [Fig. 1(a)]. They are accompanied by more extended Wannier orbitals, which are mostly associated with the wide bands and describe the more extended molecular orbitals. The topological nature of the bands forces a hybridization between the tight and extended molecular orbitals. The use of molecular orbitals is essential for the range of interactions ( $U$ ) that are large compared to the width of the flat bands ( $U > D_{\text{flat}}$ ) and small with respect to the width of the wide bands ( $U < D_{\text{wide}}$ ). Such a construction of molecular orbitals was recently achieved in a much simpler clover lattice, which also hosts a topological flat band but has only a mirror symmetry [36, 37]. The kagome lattice has considerably higher symmetry and, indeed, for a long time it has been thought that the construction of exponentially localized and Kramers-doublet Wannier orbitals is not possible [38].

From our construction, an Anderson/Kondo lattice description arises, in which the tight and

extended molecular orbitals act as effective atomic-like ( $f$ ) and conduction electron ( $c$ ) degrees of freedom. Based on this description, we uncover a continuous selective Mott transition of the molecular orbitals [Fig. 1(d)]. Associated with the transition is a metallic quantum critical point, which features the physics of Kondo destruction viewed from the Anderson/Kondo lattice perspective [25, 26, 27]. Thus, our results reveal a profound similarity of the kagome metals' metallic quantum criticality and concomitant strange metallicity with their more established heavy fermion counterparts [20, 19, 25, 26, 27]. As such, they provide an understanding of the strange-metal behavior recently observed in the kagome and related line-graph systems [28, 29, 30], and uncover a new setting for beyond-Landau quantum criticality and associated emergent quantum phases.

## Results

*Two-orbital Hubbard model on the kagome lattice:* Motivated by the electronic structure and physical properties of the line-graph materials [28, 29, 30], we consider a two-orbital Hubbard model defined on the kagome lattice which follows the crystalline space group (SG) 191. The  $C_{2z}$  and inversion symmetries allow for a spin-orbit coupling (SOC) along the  $z$  direction only, which preserves the  $U(1)$  spin- $S_z$  rotational symmetry [33]. The topological flat band, possessing a nonzero spin Chern number, is accompanied by a dispersive band above the flat band with an opposite spin Chern number. The full Hamiltonian is written as  $\mathcal{H} = \mathcal{H}_0 + \mathcal{H}_1$ , where  $\mathcal{H}_0$  is the kinetic energy term and  $\mathcal{H}_1$  describes the onsite Hubbard interaction. The band structure of  $\mathcal{H}_0$  with the parameters described in the Method is displayed in Fig. 2(a). Further details of the model are provided in the Methods and in the SM (Sec. A).

*Emergent molecular orbitals:* We proceed with the analysis of the symmetry properties of the Hamiltonian. For a set of bands, if their little-group irreducible representations (irreps) at high symmetry points can be obtained by a combination of orbitals that follows the irreps

of the site symmetry group, they are represented by some elementary band representations (EBRs) [39, 40, 41]. As such, it becomes possible to establish an “atomic limit” that adheres to the crystal symmetry and can be represented by a set of exponentially localized symmetric Wannier functions. In the present model, considering the presence of SOC, we utilize the double group to describe the symmetry representations. Doing so, we find that the wide band just below the middle flat band permits, on its own, Wannierization by symmetric exponentially localized functions. Further, the associated little group irreps for the middle two bands at high symmetry points ( $\Gamma$ ,  $K$ , and  $M$ ) are depicted in Fig. 2(b). By interchanging the irreps at the  $\Gamma$  points of these two bands, they can be transformed into EBRs that correspond to irreps of the site symmetry group at Wyckoff position  $1a$  (see the Methods and SM, Secs. A and B, for details). Consequently, these two bands can be expressed in terms of two well-defined Wannier orbitals, which are symmetric and exponentially-localized and which transform under these two specific irreps. A comprehensive analysis of the EBRs is provided in the SM, Sec. A.

We use the Wannier90 package [42] by employing trial orbital wave functions with point group symmetries that satisfy the EBR of the bands of interest to obtain both the maximally-localized Wannier orbitals and the corresponding tight binding parameters (see the SM, Sec. B, for details). The obtained Wannier functions are depicted in the SM Fig. S2(a,b). The Wannier center is at the center of the kagome lattice, leading to a tight binding model defined on the triangular lattice as illustrated in Fig 1(a). Importantly, the flat band is predominantly represented by a single Wannier orbital except in the vicinity of the  $\Gamma$  point [see Fig. 2(c)]. We therefore denote this orbital as  $WN_f$  and the other one as  $WN_c$ . We note that the orbital  $WN_f$  has the same symmetry and greatly overlaps with the flat band wavefunction in the kagome lattice model. In practice, another dispersive band, which is beneath the targeted flat band, is also close to the flat band. Because this band is topologically trivial, it can be readily Wannierized on its own. The band structure of the effective three-orbital model is shown in Fig. 2(b). At low energies,

the system flows to a single channel Kondo fixed point dictated by the conduction electron band that hybridizes more strongly with the  $f$  orbitals. In our case, the upper conduction band has a stronger hybridization because the band topology requires the Wannier functions to have weight in both bands, as shown in Fig. 2(c). We refer to the SM (Sec. E) for further details.

*Effective Anderson model and selective transition of molecular orbitals:* Importantly, and in contrast to the compact localized states, the Wannier orbitals  $WN_f$  from the different unit cells form a complete orthonormal basis (as described in detail in the SM, Sec. C). The same is true for the Wannier orbitals  $WN_c$ . Accordingly, these Wannier orbitals represent the proper molecular orbitals.

We proceed to project the Hubbard model of the original lattice to the basis of these molecular orbitals. This results in an effective model expressed as  $H_{\text{eff}} = H_0 + H_{\text{int}}$ . The kinetic term is described in detail in the Methods section and SM, Sec. D. For the interaction terms, we focus on the dominant on-site Hubbard interaction acting on the  $f$  electrons. As for the  $c$  electrons, their interactions are relatively small compared to their bandwidth and, hence, are inconsequential and can be neglected. The final form of the interaction part is given by:

$$H_{\text{int}} = \frac{u}{2} \sum_i \left( \sum_{\sigma} f_{i\sigma}^{\dagger} f_{i\sigma} - 1 \right)^2 + \sum_{ij} I_{ij} \mathbf{S}_i^f \cdot \mathbf{S}_j^f. \quad (1)$$

Here,  $f_{i\sigma}^{\dagger}$  creates an  $f$  electron with the  $WN_f$  Wannier wavefunction at the unit cell  $i$  and spin  $\sigma$ ,  $\mathbf{S}^f = f^{\dagger} \frac{\boldsymbol{\sigma}}{2} f$  is the spin operator of the  $f$  electron, and  $u$  represents the local Hubbard interaction. The Ruderman–Kittel–Kasuya–Yosida (RKKY) exchange interactions among the  $f$  electrons emerges at the low energy limit with  $I_{ij} \sim \rho_0 J_K^2 \sim \rho_0 \left( \frac{4V_{ij}^2}{u} \right)^2$ , where  $V_{ij}$  is the hybridization between the  $f$  and  $c$  electrons at the positions  $i$  and  $j$  and  $\rho_0$  is the bare density of states of the conduction electrons. To take into account the dynamical competition between the hybridization and RKKY interactions, we employ the extended dynamical mean-field theory (EDMFT) approach [43]. In this method, the correlation functions of the Anderson lattice

model are calculated in terms of a self-consistently determined Bose-Fermi Anderson (BFA) model [44, 45, 43], which couples the local moment to both bosonic and fermionic baths. The self-consistent equations governing the EDMFT calculations are described in the Methods.

We now determine the phase diagram. Without a loss of generality, we fix  $u = 0.5$  (in units of the nearest-neighbor intra-orbital hopping parameter of the original Hubbard model) and take an RKKY density of state of the form  $\rho_I(\epsilon) = \Theta(2I - |\epsilon|)/4I$  to incorporate the two-dimensional magnetic fluctuations within a kagome plane, with  $4I$  denoting the maximal amplitude of the RKKY interaction in wave vector space. We further define  $\delta = I/T_K^0$ , where  $T_K^0$  is the underlying Kondo energy scale at  $I = 0$ . Because  $\delta$  is a function of  $u$ , tuning  $\delta$  is tantamount to varying the interaction  $U$  of the original Hubbard model (Eq. 2). We perform the calculations at various temperatures to scan the phase diagram. As illustrated in Fig. 3(a), for a fixed temperature, a magnetic phase transition is indicated by the onset of the order parameter ( $m_{AF}$ ) upon increasing  $\delta$ . The incipient jump of the order parameter decreases with the lowering of temperature and is extrapolated to zero in the zero-temperature limit [43], which corresponds to a continuous quantum phase transition. Besides the suppression of magnetic order, the Anderson lattice model also undergoes a dehybridization between the  $f$  and  $c$  electrons, which is characterized by the “orbital-selective Mott” energy scale  $E_{\text{osm}}$ . The phase diagram is shown in Fig. 3. One can observe that the Néel temperature develops at the same point where the energy scale,  $E_{\text{osm}}$ , goes to zero. From the Kondo perspective, the transition corresponds to a Kondo-destruction quantum critical point. In terms of the original Hubbard model, this is a continuous selective Mott transition of the molecular orbitals.

We next turn to studying the nature of the orbital-selective Mott QCP with a special focus on its dynamical properties. We calculate both the local and lattice spin susceptibilities, which are denoted as  $\chi_{loc}(i\omega_n)$  and  $\chi(\mathbf{Q}, i\omega_n)$ , respectively (see the Methods). As shown in Fig. 4(a), at the QCP,  $\chi_{loc}(i\omega_n)$  follows a logarithmic divergence in the low frequency domain. The lattice

spin susceptibility at the magnetic ordering wavevector  $Q$  is shown in Fig. 4(b): It obeys an  $\hbar\omega/k_B T$  scaling in the quantum critical region, signifying that the quantum critical point is interacting (as opposed to Gaussian) and  $k_B T$  is the universal and only energy scale describing the quantum criticality [19]. The critical exponent for the dynamical spin susceptibility is fitted to be  $\alpha \approx 0.8$ ; the fact that it is fractional further underscores the interacting nature of the fixed point.

## Discussion

For the first time, we have theoretically realized a metallic quantum critical point enabled by the flat bands of a kagome lattice, with properties that parallel the well established strange metallicity of heavy fermion systems. The  $\hbar\omega/k_B T$  scaling implicates a linear-in- $T$  relaxation rate, which provides the understanding of the puzzling observations of the linear-in-energy damping rate in the ARPES spectrum and linear-in- $T$  resistivity in the aforementioned kagome materials [28, 29]. The dynamical scaling can be tested in future measurements of the inelastic neutron scattering cross section and optical conductivity in these systems. Finally, the selective transition of the molecular orbitals has a salient signature in a jump of Fermi surface as the system goes across the quantum critical point on the tuning axis  $\delta$ . This theoretical expectation can be tested by ARPES, Hall effect and quantum oscillation measurements in the aforementioned line-graph materials in the low-temperature regime (once the experimental tuning axes are established that go across the QCP), by analogy with the well-established Hall and quantum oscillation measurements in quantum critical heavy fermion metals [22, 23, 24]. The quantum criticality we have uncovered is closely related to the Kondo-destruction quantum criticality. As such, the orbital-selective Mott criticality enabled by the flat bands represents a new platform for realizing and probing beyond-Landau quantum criticality [19, 20, 22, 23, 24, 25, 26, 27].

The orbital-selective Mott criticality is also expected to promote emergent quantum phases.



A promising emergent phase is superconductivity. By analogy with the case of heavy-fermion quantum criticality [46], we can expect the superconductivity to have a high transition temperature (as measured by the natural underlying Fermi temperature scale). Our work, thus, raises the prospect for the development of unconventional superconductivity in kagome metals.

Going beyond kagome metals, our results make it natural for the flat bands in other line-graph settings, such as the pyrochlore lattice, to enable a similar form of quantum criticality. In turn, this provides an understanding of the recent experimental observation of strange metallicity in a pyrochlore metal [30]. More generally, our work showcases the link between the transition-metal line-graph metals, heavy fermions and moiré systems, where a Kondo perspective has also been theoretically fruitful [47, 48, 49, 50, 51] and where strange-metal behavior is being experimentally uncovered [52, 53, 54].

In conclusion, we have advanced a realistic model study on the effect of local Coulomb interactions in the flat bands of a kagome metal. We have constructed the molecular orbitals, which, in contrast to the compact localized states, form a proper basis. This leads to an Anderson/Kondo lattice description for the selective correlations of the molecular orbitals, which in turn allows a non-perturbative study that uncovers a continuous selective transition of the molecular orbitals. The resulting quantum critical metal has the hallmarks of strange metallicity. Our work allows the first theoretical understanding of the emerging experiments on strange metal behavior in line-graph materials, predicts accompanying properties in single-electron excitations and collective dynamics, and raises the prospect for unconventional superconductivity in these systems. Our findings also reveal new interconnections among a variety of correlated electron platforms, and point to new platforms for beyond-Landau quantum criticality.

## Methods

*Hubbard model on the kagome lattice:* The kagome lattice contains three sublattices. The site symmetry group for each sublattice is  $D_{2h}$ , and the local orbitals can be classified into orbitals of even and odd according to the eigenvalues of the  $C_{2z}$  symmetry (see the details in the SM, Sec. A). For the physical  $3d$ -orbitals of the transition-metal systems, there are two classes according to the  $C_{2z}$  symmetry: The  $3d_{z^2}/3d_{xy}/3d_{x^2-y^2}$  orbitals are even, while the  $3d_{xz}/3d_{yz}$  orbitals are odd under  $C_{2z}$ . We consider a two-orbital model defined on the kagome lattice, with one even and one odd  $3d$  orbital denoted as  $\psi_1$  and  $\psi_2$  respectively. It is written as  $\mathcal{H} = \mathcal{H}_0 + \mathcal{H}_1$ , which contains the on-site Hubbard interaction,

$$\mathcal{H}_1 = \frac{U}{2} \sum_{i,\eta} \left( \sum_{\tau\sigma} n_{i,\eta,\tau,\sigma} - 2 \right)^2 \quad (2)$$

where  $\tau = 1, 2$  and  $\sigma = (\uparrow, \downarrow)$  denote the orbital and spin indices, respectively, and  $\eta = A/B/C$  goes through the three sublattices in a unit cell. The kinetic Hamiltonian is given by  $\mathcal{H}_0 = \sum_{\mathbf{k}\sigma} \Psi_{\mathbf{k}\sigma}^\dagger \mathcal{H}_0^\sigma(\mathbf{k}) \Psi_{\mathbf{k}\sigma}$ , where  $\Psi_{\mathbf{k}\sigma} = [\psi_{A\tau\sigma}, \psi_{B\tau\sigma}, \psi_{C\tau\sigma}]^T$ . As described earlier, there only exists spin-orbital coupling along the  $z$  direction; thus,  $\mathcal{H}_0^\uparrow(\mathbf{k}) = [\mathcal{H}_0^\downarrow(\mathbf{k})]^*$  [33] and

$$\mathcal{H}_0^\uparrow(\mathbf{k}) = \begin{pmatrix} \mathcal{H}_0^{11}(\mathbf{k}) & \mathcal{H}_0^{12}(\mathbf{k}) \\ [\mathcal{H}_0^{12}(\mathbf{k})]^\dagger & \mathcal{H}_0^{22}(\mathbf{k}) \end{pmatrix}, \quad (3)$$

where

$$\mathcal{H}_0^{\tau\tau}(\mathbf{k}) = \begin{pmatrix} -\epsilon_\tau & 2(-t_\tau + i\lambda_\tau) \cos k_1 & 2(-t_\tau - i\lambda_\tau) \cos k_2 \\ 2(-t_\tau - i\lambda_\tau) \cos k_1 & -\epsilon_\tau & 2(-t_\tau + i\lambda_\tau) \cos k_3 \\ 2(-t_\tau + i\lambda_\tau) \cos k_2 & 2(-t_\tau - i\lambda_\tau) \cos k_3 & -\epsilon_\tau \end{pmatrix}, \quad (4)$$

and

$$\mathcal{H}_0^{12}(\mathbf{k}) = \begin{pmatrix} 0 & -2it_{12} \sin k_1 & 2it_{21} \sin k_2 \\ -2it_{21} \sin k_1 & 0 & -2it_{12} \sin k_3 \\ 2it_{12} \sin k_2 & -2it_{21} \sin k_3 & 0 \end{pmatrix}. \quad (5)$$

The basis vectors of the kagome lattice are  $\mathbf{a}_{1/2} = \frac{1}{2}\mathbf{x} \pm \frac{\sqrt{3}}{2}\mathbf{y}$ . In addition,  $\mathbf{d}_1 = \frac{1}{2}(\mathbf{a}_1 + \mathbf{a}_2)$ ,  $\mathbf{d}_2 = \frac{1}{2}\mathbf{a}_1$ ,  $\mathbf{d}_3 = -\frac{1}{2}\mathbf{a}_2$  are the displacements between the different sublattices, and  $k_i = \mathbf{k} \cdot \mathbf{d}_i$

[Fig. S1(b) and (c)]. Furthermore,  $t_\tau$  and  $\lambda_\tau$  denote the nearest-neighbor intraorbital hopping and spin-orbital coupling respectively,  $\epsilon_\tau$  is the energy level for the orbital  $\tau$ , and  $t_{12}/t_{21}$  are the symmetry-allowed interorbital hoppings. Without a loss of generality, we adapt the following parameter setting with  $t_1 = t_2 = 1$ ,  $\lambda_1 = \lambda_2 = -0.18$ ,  $\epsilon_1 = -2.75$ ,  $\epsilon_2 = 4.25$  and  $t_{12} = t_{21} = -0.1$ . A detailed analysis of the dispersion and symmetry is provided in the SM, Sec. A.

*Effective extended Anderson model on the Wannier basis:* We focus on the flat and dispersive bands close to the Fermi energy. By interchanging the irreps at the  $\Gamma$  points of these two bands, we find that they develop into the induced representations  $\bar{E}_{1g} \uparrow G$  and  $\bar{E}_{1u} \uparrow G$  [55], where  $\bar{E}_{1g}$  and  $\bar{E}_{1u}$  are the site symmetry group irreps at Wyckoff position  $1a$ . In other words, these two bands can be represented by a set of exponentially localized Wannier orbitals, which transform as these site symmetry group irreps, without topological obstruction (See the SM, Secs. A and B). The Wannier centers of the emergent orbitals turn out to form a triangular lattice. The flat band is mostly captured by one orbital, which we call  $WN_f$ , while the dispersive band is mostly represented by the other one which we name  $WN_c$ . We project the Hubbard model of the original lattice to the Wannier basis. This leads to an effective Anderson model expressed in terms of the  $f$  and  $c$  electrons with  $H_{eff} = H_0 + H_{int}$ . Here, the kinetic term is:

$$\begin{aligned}
H_0 &= H_f + H_c + H_v \\
&= \sum_{ij,\sigma} t_{ij}^f \left( f_{i\sigma}^\dagger f_{j\sigma} + h.c. \right) - \sum_i \epsilon_f f_{i\sigma}^\dagger f_{i\sigma} \\
&+ \sum_{ij,\sigma} t_{ij}^c \left( c_{i\sigma}^\dagger c_{j\sigma} + h.c. \right) - \sum_{i\sigma} \epsilon_c c_{i\sigma}^\dagger c_{i\sigma} \\
&+ \sum_{ij\sigma} \left( V_{ij}^\sigma f_{i\sigma}^\dagger c_{j\sigma} + h.c. \right).
\end{aligned} \tag{6}$$

Here,  $f_{i\sigma}^\dagger$  ( $c_{i\sigma}^\dagger$ ) creates a heavy (light) electron at the position  $i$  with spin  $\sigma$ ,  $t_{ij}^f$  ( $t_{ij}^c$ ) describes the hopping among the  $f$  ( $c$ ) electrons between the positions  $i$  and  $j$ , and the  $|t^f|$ 's, the hopping amplitudes between the  $f$  orbitals, are much smaller than the  $|t^c|$ 's, the hopping amplitudes between the  $c$  orbitals. In addition,  $V_{ij}^\sigma$  represents the hybridization between the light and heavy

orbitals. According to time reversal symmetry,  $V_{ij}^\dagger = (V_{ij}^\downarrow)^*$ . Finally,  $\epsilon_c$  ( $\epsilon_f$ ) denotes the energy level of the  $c$  ( $f$ ) orbital in the noninteracting limit.

*Extended dynamical mean field theory and self-consistent equations:* The EDMFT method can be used to analyze the dynamical competition between the hybridization and RKKY interactions. We treat the model  $H_{eff}$  with EDMFT by calculating the correlation functions of the lattice model in terms of an effective Bose-Fermi Anderson (BFA) model:

$$S_{BFA} = \sum_{\omega, \sigma, a, b} \phi_{a, \sigma}^\dagger [(-i\omega_n - \epsilon)\delta_{ab} + \Delta_{ab}(i\omega_n)] \phi_{b, \sigma} - \frac{1}{2} \sum_{\Omega, \nu=x, y, z} S^\nu(i\Omega_n) \chi_0^{\nu, -1}(i\Omega_n) S^\nu(-i\Omega) + \int_\tau d\tau h_0, \quad (7)$$

where  $\epsilon = \text{diag}(\epsilon_f, \epsilon_c)$  is the energy levels written in a matrix form. In the BFA model, the local orbitals are coupled to both the fermionic baths  $[\Delta(i\omega_n)]$  and the bosonic bath  $[\chi_0^\mu(i\Omega_n)]$ , which capture the dynamics of the hybridization and spin correlations, respectively. The bath functions  $\Delta(i\omega_n)$  and  $\chi_0^{\nu, -1}$  are determined via the following self-consistent equations:

$$G_{loc}(i\omega_n) = \sum_{\mathbf{k}} [i\omega_n - H_0(\mathbf{k}) - \Sigma(i\omega_n)]^{-1} = [(i\omega_n + \epsilon - \Delta(i\omega_n))^{-1} - \Sigma(i\omega_n)]^{-1}, \quad (8)$$

$$\chi_{loc}^\nu(i\Omega_n) = \sum_{\mathbf{q}} [J_{\mathbf{q}}^\nu + M^\nu(i\Omega_n)]^{-1} = [\chi_0^{\nu, -1}(i\Omega) + M^\nu(i\Omega_n)]^{-1}.$$

Here,  $G_{loc}(i\omega_n)$  and  $\chi_{loc}^\nu(i\Omega_n)$  are the single-particle Green's function of the local cluster and the local spin-spin correlation functions,  $\Sigma(i\omega_n)$  and  $M^\nu(i\Omega_n)$  are the self-energy and spin cumulant, respectively. Because the  $f$  and  $c$  orbitals belong to different irreducible representations, the on-site hopping between the orbitals is forbidden. Therefore  $G_{loc}(i\omega_n)$ ,  $\Sigma(i\omega_n)$  and  $\Delta(i\omega_n)$  are block diagonal [56, 57]. As the spatial spin interactions of the  $f$  orbitals are predominant and are considered, only the  $f$  orbital is coupled with the bosonic bath in the BFA. The existence of the SOC induces spin anisotropy. The precise form of spin anisotropy is unimportant, recognizing that the emergence of new fixed points in the Bose-Fermi Anderson/Kondo

model is insensitive to the spin symmetry [19, 44]. For simplicity, we consider the spatial spin interactions to be Ising anisotropic, with the RKKY interaction to be  $I \sum_{\langle ij \rangle} S_{f,i}^z S_{f,j}^z$ .

*Local and lattice dynamical spin susceptibilities:* We first define the dynamical local spin susceptibility as

$$\chi_{loc}^{\nu}(i\omega_n, T) = \int_0^{\beta} d\tau e^{i\omega_n \tau} \langle S^{\nu}(\tau) S^{\nu}(0) \rangle, \quad (9)$$

where  $S$  is the spin of the impurity model with the spin direction  $\nu = x, y, z$ . As shown in Fig. 4(a), at the OSM QCP, the isothermal local spin susceptibility follows a logarithmic function as

$$\chi_{loc}(i\omega_n) = \frac{-\alpha_{\omega}}{4I} \log \omega_n. \quad (10)$$

The lattice spin susceptibility is determined by the Dyson equation:

$$\chi^{\alpha}(\mathbf{q}, i\omega) = \frac{1}{M^{\alpha}(i\omega) + I_{\mathbf{q}}}, \quad (11)$$

with  $\alpha \in x, y, z$ . At the magnetic wave vector  $\mathbf{Q}$ , we have

$$\chi^{\alpha}(\mathbf{Q}, i\omega_n) = \frac{1}{M^{\alpha}(i\omega_n) - 2I}. \quad (12)$$

Combining this equation with the self-consistent equations in Eq. 8, we have the following asymptotic form when  $4I\chi_{loc} \gg 1$ ,

$$\chi^{\alpha}(\mathbf{Q}, i\omega) \approx \frac{\exp(4I\chi_{loc}^{\alpha}(i\omega_n))}{4I}. \quad (13)$$

**Data availability:** All data needed to evaluate the conclusions in the paper are presented in the paper and/or the Supplementary Materials. Additional data that have been used are available from the corresponding author.

## References

- [1] Keimer, B. & Moore, J. E. The physics of quantum materials. *Nat. Phys.* **13**, 1045 (2017).

- [2] Paschen, S. & Si, Q. Quantum phases driven by strong correlations. *Nat. Rev. Phys.* **3**, 9 (2021).
- [3] Imada, M., Fujimori, A. & Tokura, Y. Metal-insulator transitions. *Rev. Mod. Phys.* **70**, 1039–1263 (1998).
- [4] Coleman, P. & Schofield, A. J. Quantum criticality. *Nature* **433**, 226 (2005).
- [5] Si, Q. & Steglich, F. Heavy fermions and quantum phase transitions. *Science* **329**, 1161–1166 (2010).
- [6] Bistritzer, R. & MacDonald, A. H. Moiré bands in twisted double-layer graphene. *Proc. Natl. Acad. Sci. U.S.A.* **108**, 12233–12237 (2011).
- [7] Cao, Y. *et al.* Unconventional superconductivity in magic-angle graphene superlattices. *Nature* **556**, 43–50 (2018).
- [8] Mielke, A. Ferromagnetic ground states for the Hubbard model on line graphs. *J. Phys. A: Math. Gen.* **24**, L73 (1991).
- [9] Ye, L. *et al.* Massive Dirac fermions in a ferromagnetic kagome metal. *Nature* **555**, 638–642 (2018).
- [10] Yao, M. *et al.* Switchable Weyl nodes in topological kagome ferromagnet  $\text{Fe}_3\text{Sn}_2$ . *arXiv:1810.01514* (2018).
- [11] Kang, M. *et al.* Topological flat bands in frustrated kagome lattice  $\text{CoSn}$ . *Nat. Commun.* **11**, 1–9 (2020).
- [12] Jiang, Y.-X. *et al.* Unconventional chiral charge order in kagome superconductor  $\text{KV}_3\text{Sb}_5$ . *Nat. Mater.* **20**, 1353 (2021).

- [13] Mielke, C. *et al.* Time-reversal symmetry-breaking charge order in a correlated kagome superconductor. *Nature* **602**, 245–250 (2022).
- [14] Zhou, S. & Wang, Z. Chern Fermi pocket, topological pair density wave, and charge-4e and charge-6e superconductivity in kagome superconductors. *Nat. Commun.* **13**, 7288 (2022).
- [15] Teng, X. *et al.* Discovery of charge density wave in a correlated kagome lattice antiferromagnet. *Nature* 490–495 (2022).
- [16] Yin, J.-X. *et al.* Discovery of charge order and corresponding edge state in kagome magnet FeGe. *Phys. Rev. Lett.* **129**, 166401 (2022).
- [17] Setty, C. *et al.* Electron correlations and charge density wave in the topological kagome metal FeGe. *arXiv preprint arXiv:2203.01930* (2022).
- [18] Phillips, P. W., Hussey, N. E. & Abbamonte, P. Stranger than metals. *Science* **377**, eabh4273 (2022).
- [19] Hu, H., Chen, L. & Si, Q. Quantum critical metals: Dynamical planckian scaling and loss of quasiparticles. *arXiv preprint arXiv:2210.14183* (2022).
- [20] Kirchner, S. *et al.* Colloquium: Heavy-electron quantum criticality and single-particle spectroscopy. *Rev. Mod. Phys.* **92**, 011002 (2020).
- [21] Löhneysen, H. v., Rosch, A., Vojta, M. & Wölfle, P. Fermi-liquid instabilities at magnetic quantum phase transitions. *Rev. Mod. Phys.* **79**, 1015–1075 (2007).
- [22] Paschen, S. *et al.* Hall-effect evolution across a heavy-fermion quantum critical point. *Nature* **432**, 881 (2004).

- [23] Shishido, H., Settai, R., Harima, H. & Ōnuki, Y. A drastic change of the Fermi surface at a critical pressure in CeRhIn<sub>5</sub>: dHvA study under pressure. *J. Phys. Soc. Jpn.* **74**, 1103–1106 (2005).
- [24] Park, T. *et al.* Hidden magnetism and quantum criticality in the heavy fermion superconductor CeRhIn<sub>5</sub>. *Nature* **440**, 65–68 (2006).
- [25] Si, Q., Rabello, S., Ingersent, K. & Smith, J. L. Locally critical quantum phase transitions in strongly correlated metals. *Nature* **413**, 804–808 (2001).
- [26] Coleman, P., Pépin, C., Si, Q. & Ramazashvili, R. How do Fermi liquids get heavy and die? *J. Phys. Cond. Matt.* **13**, R723 (2001).
- [27] Senthil, T., Vojta, M. & Sachdev, S. Weak magnetism and non-fermi liquids near heavy-fermion critical points. *Phys. Rev. B* **69**, 035111 (2004).
- [28] Ye, L. *et al.* A flat band-induced correlated kagome metal. *arXiv:2106.10824* (2021).
- [29] Ekahana, S. A. *et al.* Anomalous quasiparticles in the zone center electron pocket of the kagome ferromagnet Fe<sub>3</sub>Sn<sub>2</sub>. *arXiv:2206.13750* (2022).
- [30] Huang, J. *et al.* Non-Fermi liquid behavior in a correlated flatband pyrochlore. *preprint* (2023).
- [31] Leykam, D., Andreanov, A. & Flach, S. Artificial flat band systems: from lattice models to experiments. *Adv. Phys.: X* **3**, 1473052 (2018).
- [32] Bergman, D. L., Wu, C. & Balents, L. Band touching from real-space topology in frustrated hopping models. *Phys. Rev. B* **78**, 125104 (2008).



- [33] Tang, E., Mei, J.-W. & Wen, X.-G. High-temperature fractional quantum hall states. *Phys. Rev. Lett.* **106**, 236802 (2011).
- [34] Ma, D.-S. *et al.* Spin-orbit-induced topological flat bands in line and split graphs of bipartite lattices. *Phys. Rev. Lett.* **125**, 266403 (2020).
- [35] Soluyanov, A. A. & Vanderbilt, D. Wannier representation of  $Z_2$  topological insulators. *Phys. Rev. B* **83**, 035108 (2011).
- [36] Hu, H. & Si, Q. Coupled topological flat and wide bands: Quasiparticle formation and destruction. *Sci. Adv.* **9**, eadg0028 (2023).
- [37] Chen, L. *et al.* Emergent flat band and topological kondo semimetal driven by orbital-selective correlations. *arXiv preprint arXiv:2212.08017* (2022).
- [38] Huber, S. D. & Altman, E. Bose condensation in flat bands. *Phys. Rev. B* **82**, 184502 (2010).
- [39] Bradlyn, B. *et al.* Topological quantum chemistry. *Nature* **547**, 298–305 (2017).
- [40] Cano, J. *et al.* Building blocks of topological quantum chemistry: Elementary band representations. *Phys. Rev. B* **97**, 035139 (2018).
- [41] Cano, J. & Bradlyn, B. Band representations and topological quantum chemistry. *Annu. Rev. Condens. Matter Phys.* **12**, 225–246 (2021).
- [42] Pizzi, G. *et al.* Wannier90 as a community code: new features and applications. *J. Phys. Condens. Matter.* **32**, 165902 (2020).
- [43] Hu, H., Chen, L. & Si, Q. Extended dynamical mean field theory for correlated electron models. *arXiv preprint arXiv:2210.14197* (2022).

- [44] Zhu, L. & Si, Q. Critical local-moment fluctuations in the Bose-Fermi Kondo model. *Phys. Rev. B* **66**, 024426 (2002).
- [45] Cai, A. & Si, Q. Bose-Fermi Anderson model with SU(2) symmetry: Continuous-time quantum Monte Carlo study. *Phys. Rev. B* **100**, 014439 (2019).
- [46] Hu, H. *et al.* Unconventional superconductivity from Fermi surface fluctuations in strongly correlated metals. *arXiv preprint arXiv:2109.13224* (2021).
- [47] Ramires, A. & Lado, J. L. Emulating heavy fermions in twisted trilayer graphene. *Phys. Rev. Lett.* **127**, 026401 (2021).
- [48] Song, Z.-D. & Bernevig, B. A. Magic-angle twisted bilayer graphene as a topological heavy fermion problem. *Phys. Rev. Lett.* **129**, 047601 (2022).
- [49] Kumar, A., Hu, N. C., MacDonald, A. H. & Potter, A. C. Gate-tunable heavy fermion quantum criticality in a moiré Kondo lattice. *Phys. Rev. B* **106**, L041116 (2022).
- [50] Guerci, D. *et al.* Chiral Kondo lattice in doped MoTe<sub>2</sub>/WSe<sub>2</sub> bilayers. *arXiv preprint arXiv:2207.06476* (2022).
- [51] Zhao, W. *et al.* Gate-tunable heavy fermions in a moiré Kondo lattice. *Nature* **616**, 61–65 (2023).
- [52] Cao, Y. *et al.* Strange metal in magic-angle graphene with near planckian dissipation. *Phys. Rev. Lett.* **124**, 076801 (2020).
- [53] Ghiotto, A. *et al.* Quantum criticality in twisted transition metal dichalcogenides. *Nature* **597**, 345–349 (2021).

- [54] Jaoui, A. *et al.* Quantum critical behaviour in magic-angle twisted bilayer graphene. *Nat. Phys.* **18**, 633–638 (2022).
- [55] Inui, T., Tanabe, Y. & Onodera, Y. *Group theory and its applications in physics*, vol. 78 (2012).
- [56] Kugler, F. B. & Kotliar, G. Is the orbital-selective mott phase stable against interorbital hopping? *Phys. Rev. Lett.* **129**, 096403 (2022).
- [57] Hu, H., Chen, L., Zhu, J.-X., Yu, R. & Si, Q. Orbital-selective mott phase as a dehybridization fixed point. *arXiv preprint arXiv:2203.06140* (2022).
- [58] Aroyo, M. I. *et al.* Crystallography online: Bilbao crystallographic server. *Bulg. Chem. Commun* **43**, 183–197 (2011).
- [59] Marzari, N., Mostofi, A. A., Yates, J. R., Souza, I. & Vanderbilt, D. Maximally localized Wannier functions: Theory and applications. *Rev. Mod. Phys.* **84**, 1419–1475 (2012).

**Acknowledgment:** We thank Gabriel Aeppli, Joseph Checkelsky, and Ming Yi for useful discussions. Work at Rice has primarily been supported by the U.S. DOE, BES, under Award No. DE-SC0018197 (Conceptualization and Wannier construction, L.C. and F.X.), by the Air Force Office of Scientific Research under Grant No. FA9550-21-1-0356 (Conceptualization and orbital-selective transition, L.C., F.X., S.S.), and by the Robert A. Welch Foundation Grant No. C-1411 (Q.S.). The majority of the computational calculations have been performed on the Shared University Grid at Rice funded by NSF under Grant EIA-0216467, a partnership between Rice University, Sun Microsystems, and Sigma Solutions, Inc., the Big-Data Private-Cloud Research Cyberinfrastructure MRI-award funded by NSF under Grant No. CNS-1338099, and the Extreme Science and Engineering Discovery Environment (XSEDE) by NSF under Grant No. DMR170109. H.H. acknowledges the support of the European Research Council (ERC) under the European Union’s Horizon 2020 research and innovation program (Grant Agreement No. 101020833). Work in Vienna was supported by the Austrian Science Fund (projects I 5868-N - FOR 5249 - QUAST and and SFB F 86, Q-M&S) and the ERC (Advanced Grant CorMeTop, No. 101055088). J.C. acknowledges the support of the National Science Foundation under Grant No. DMR-1942447, support from the Alfred P. Sloan Foundation through a Sloan Research Fellowship and the support of the Flatiron Institute, a division of the Simons Foundation. Six of us (L.C., F.X., S.S., S.P., J.C., Q.S.) acknowledge the hospitality of the Kavli Institute for Theoretical Physics, supported in part by the National Science Foundation under Grant No. NSF PHY1748958, during the program “A Quantum Universe in a Crystal: Symmetry and Topology across the Correlation Spectrum”. S.S., J.C., S.P. and Q.S. acknowledge the hospitality of the Aspen Center for Physics, which is supported by NSF grant No. PHY-2210452.

**Author contributions:** Q.S. conceived the research. L.C., F.X., S.S., H.H., J.C. and Q.S. carried out model studies. S.P., J.C. and Q.S. provided insights into the flat band and Kondo

systems. L.C. and Q.S. wrote the manuscript, with inputs from all authors.

**Competing interests:** The authors declare no competing interests.

**Additional information:** Correspondence and requests for materials should be addressed to Q.S. (qmsi@rice.edu).

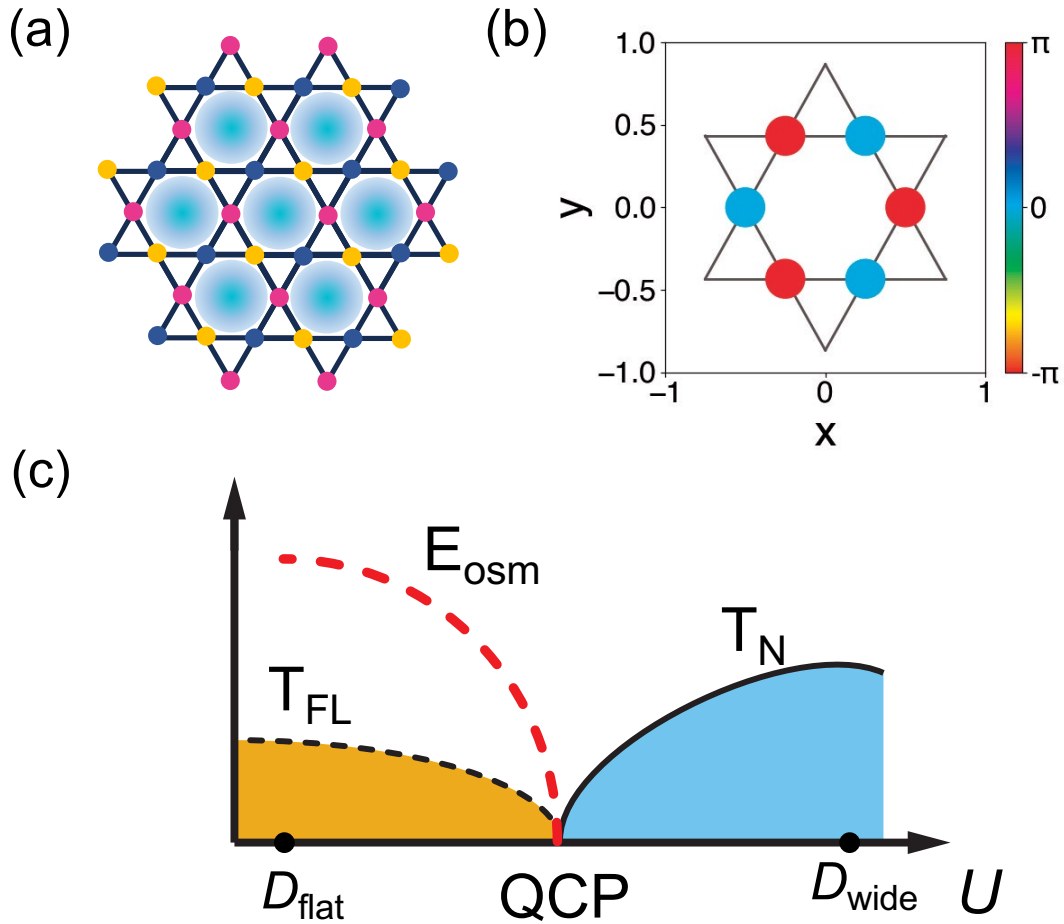


Figure 1: **Illustration of the lattice geometry, compact localized state, Wannier centers, and the qualitative phase diagram.** **a**, Geometry of the kagome lattice with three sites per unit cell. The Wannier centers of the emergent Wannier orbitals are marked by the light-blue circles (centered at Wyckoff position 1a). **b**, The real space representation of the compact localized state for the flat band in the single orbital kagome system. **c**, The qualitative phase diagram featuring a selective Mott transition of the molecular orbitals, with an associated energy scale for “orbital-selective Mott” (osm) crossover (that turns into a phase transition at zero temperature).

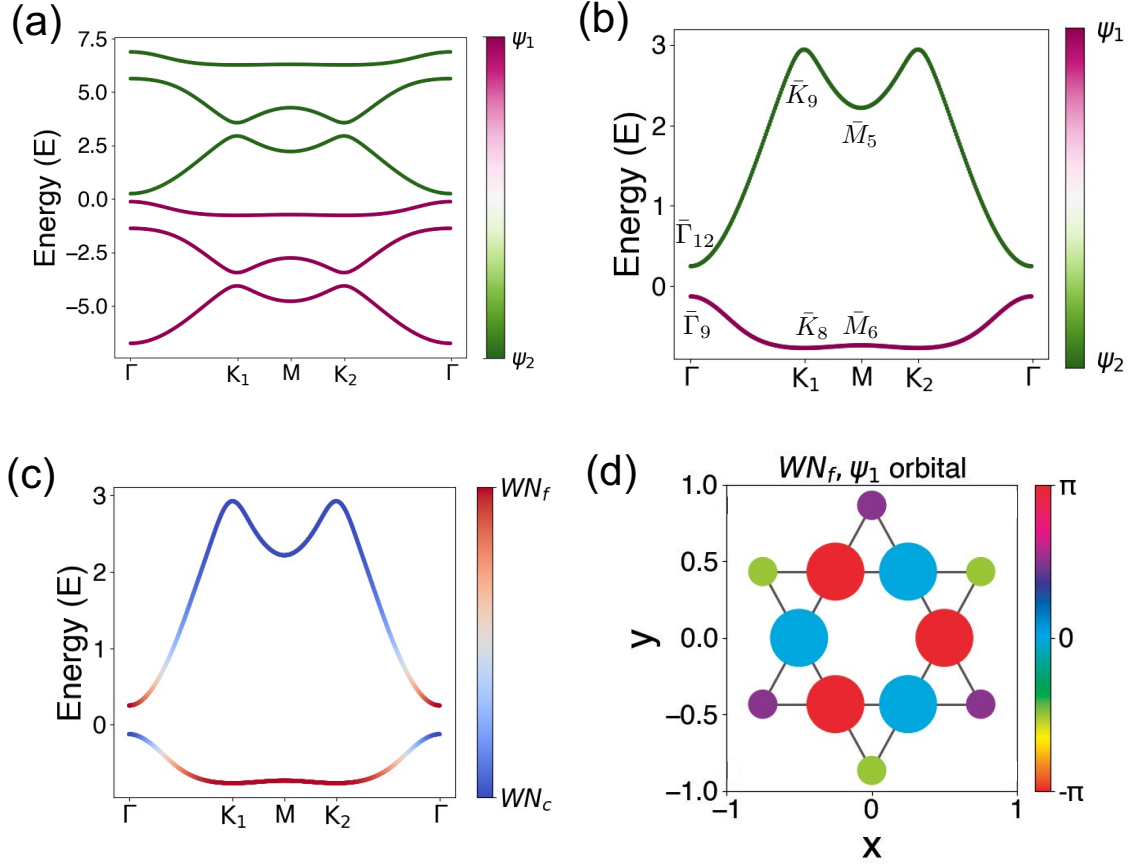


Figure 2: **Noninteracting bandstructure.** **a**, The band structure of the two-orbital model in the original kagome lattice, with the parameter setting described in the Methods. **b**, The band structure for the middle two bands in the original Hamiltonian. The little group representations at high symmetry points are marked. **c**, The dispersion of the effective Hamiltonian using two Wannier orbitals, with the color indicating the ratio of the Wannier orbital components. **d**, The shape of the Wannier orbital for  $WN_f$  ( $\psi_1$  component) in real space. The size (color) of the dot indicates the square root of the density (phase) of the Wannier function. (The density of the Wannier function is defined as  $|w(r)|^2$ .)

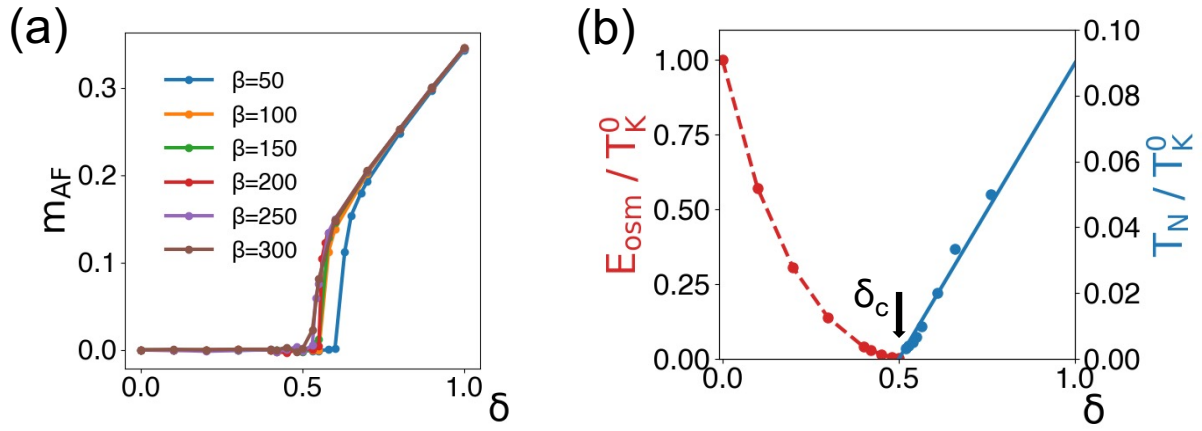


Figure 3: **Phase diagram and the orbital-selective Mott energy scale.** **a**, The amplitude of the antiferromagnetic (AF) order parameter  $m_{AF}$  vs. the tuning parameter  $\delta$ , which characterizes the dependence on the effective Hubbard interaction  $u$  of the RKKY interaction to the Kondo scale ratio. **b**, Phase diagram showing how the Néel temperature  $T_N$  and the orbital-selective Mott energy scale  $E_{osm}$  evolve with  $\delta$ .



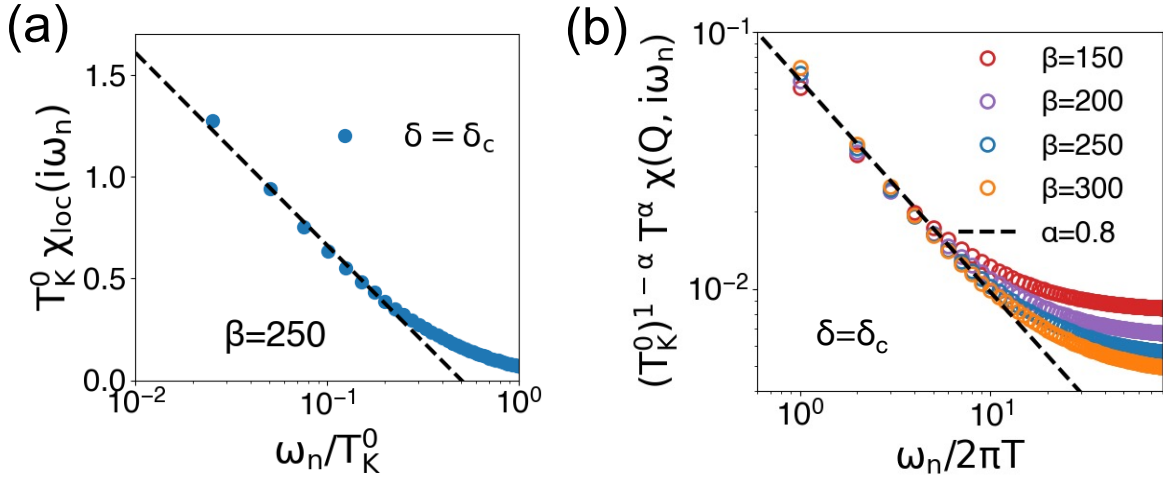


Figure 4: **Dynamical scaling at the metallic quantum critical point.** **a**, The dynamical local spin susceptibility at the QCP ( $\delta = \delta_c$ ). **b**,  $\hbar\omega/k_B T$  scaling for the dynamical lattice spin susceptibility, also at the QCP. Here, in the figure legends,  $\hbar$  and  $k_B$  have been set to 1.

# Supplementary Materials

## Metallic quantum criticality enabled by flat bands in a kagome lattice

Lei Chen, Fang Xie, Shouvik Sur, Haoyu Hu, Silke Paschen, Jennifer Cano, Qimiao Si

Figs. S1 to S7

Tables S1 to S5

References (25,35,36, 42,58,59, see the above)

### A. Symmetry analysis and band structure in the original Hamiltonian

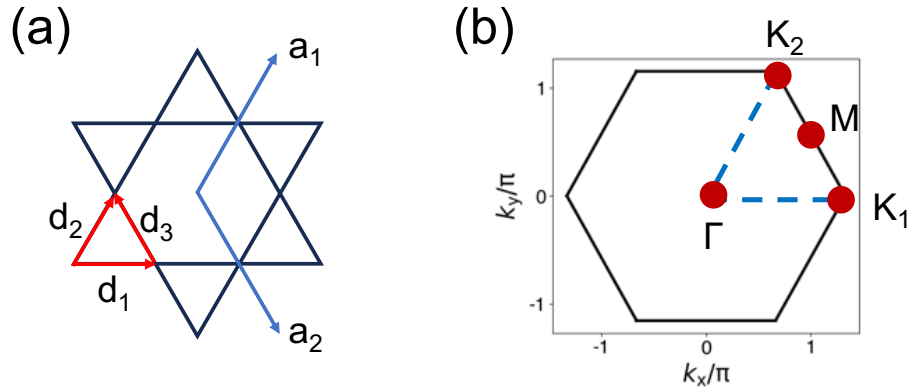


Figure S1: **Lattice structure.** **a**, The kagome lattice, with the basis vectors  $\mathbf{a}_1 = \frac{1}{2}\hat{x} + \frac{\sqrt{3}}{2}\hat{y}$  and  $\mathbf{a}_2 = \frac{1}{2}\hat{x} - \frac{\sqrt{3}}{2}\hat{y}$ . Here  $\hat{x}$  and  $\hat{y}$  represent the unit vectors in Cartesian coordinate. The displacements between the sublattices are denoted by  $d_i$ . **b**, The first Brillouin zone of the kagome lattice, with some high symmetry points in the Brillouin zone marked.

The non-interacting Hamiltonian governing the model on the original kagome lattice is de-

scribed by Eqs. (3-5) (see the Methods). This model exhibits crystalline symmetry characterized by the space group  $P6/mmm$  (SG191), which preserves both the time reversal and inversion symmetries. Consequently, the bands possess a twofold degeneracy throughout the Brillouin zone (BZ). Moreover, the  $C_{2z}$  symmetry on the kagome lattice prevents any in-plane SOC, thereby maintaining the  $U(1)$  spin rotational symmetry. As a result, the spin-up and spin-down sectors can be treated independently. At each kagome sublattice, which has a  $D_{2h}$  site symmetry group, we include two orbitals that transform as  $\bar{E}_g$  and  $\bar{E}_u$  irreps. They are denoted as  $\psi_1$  and  $\psi_2$  respectively.

We next turn to wave vector space and discuss the little-group representations at high symmetry points. To analyze the EBRs, we utilize the notation provided by the BANDREP application of the Bilbao Crystallographic Server (BCS) [58]. The irreps in  $\bar{E}_g \uparrow G$  and  $\bar{E}_u \uparrow G$  from Wyckoff position  $3f$  are  $(\bar{\Gamma}_7, \bar{\Gamma}_8, \bar{\Gamma}_9, \bar{K}_7, \bar{K}_8, \bar{K}_9, \bar{M}_5, 2\bar{M}_6)$  and  $(\bar{\Gamma}_{10}, \bar{\Gamma}_{11}, \bar{\Gamma}_{12}, \bar{K}_7, \bar{K}_8, \bar{K}_9, 2\bar{M}_5, \bar{M}_6)$ , respectively. The specific energy order of these irreps are dependent on the parameters of the tight-binding model. However, as we gradually reduce the strength of the SOC, the band structure should converge to that of the simplest spinless kagome model with a nearest-neighbor hopping, which has band touching points corresponding to two dimensional irreps. Therefore, when the SOC is smaller than the nearest-neighbor hopping strength, we observe certain relative energy relations in the EBRs. Specifically, for  $\bar{E}_g \uparrow G$ ,  $\bar{\Gamma}_9$  is closer to  $\bar{\Gamma}_7$ , and  $\bar{K}_7$  is closer to  $\bar{K}_9$ . Similarly, for  $\bar{E}_u \uparrow G$ ,  $\bar{\Gamma}_{11}$  is closer to  $\bar{\Gamma}_{10}$  and  $\bar{K}_7$  is closer to  $\bar{K}_9$ .

We have determined the irreps at each high symmetry point. The corresponding results are summarized in Table 1. Each row of the table provides information about the irreps at high symmetry points of the isolated double degenerate bands, ordered from the top to the bottom according to the energy hierarchy as depicted in Fig. 2(a).

Wyckoff	EBRs	$\Gamma$ irreps	$K$ irreps	$M$ irreps
3 <i>f</i>	$\bar{E}_u \uparrow G$	$\bar{\Gamma}_{11}$	$\bar{K}_8$	$\bar{M}_5$
		$\bar{\Gamma}_{10}$	$\bar{K}_7$	$\bar{M}_6$
		$\bar{\Gamma}_{12}$	$\bar{K}_9$	$\bar{M}_5$
	$\bar{E}_g \uparrow G$	$\bar{\Gamma}_9$	$\bar{K}_8$	$\bar{M}_6$
		$\bar{\Gamma}_7$	$\bar{K}_7$	$\bar{M}_5$
		$\bar{\Gamma}_8$	$\bar{K}_9$	$\bar{M}_6$

Table 1: Band representations and the corresponding irreps at high symmetry points for the spinful Hamiltonian that follows SG191 with orbitals at Wyckoff position 3*f*. Each row corresponds to the irreps of an isolated energy band, and the ordering is associated with the bands in Fig. 2(a).

Wyckoff	EBRs	$\Gamma$ irreps	$K$ irreps	$M$ irreps
1 <i>a</i>	$\bar{E}_{1u} \uparrow G$	$\bar{\Gamma}_{12}$	$\bar{K}_8$	$\bar{M}_6$
	$\bar{E}_{1g} \uparrow G$	$\bar{\Gamma}_9$	$\bar{K}_9$	$\bar{M}_5$

Table 2: EBRs and the connection relation for SG191 at Wyckoff 1*a*.

## B. Wannier construction

We focus on the middle two bands and construct the Wannier orbitals. Individually, each of the middle two bands has nonzero spin Chern number and, thus, suffers from topological obstruction [35]. However, this obstruction can be circumvented if we Wannierize them together. This can be understood, if we switch over the irreps at the  $\Gamma$  point for the middle two bands. As shown in Table 2, after the exchange, the new sets of the little group irreps follow the EBRs  $\bar{E}_{1g} \uparrow G$  and  $\bar{E}_{1u} \uparrow G$  at Wyckoff position 1*a*, respectively. In other words, we can construct two Wannier orbitals, whose symmetry transformation follows  $\bar{E}_{1g}$  and  $\bar{E}_{1u}$  irreps, to represent the middle two bands. A distinct feature of these Wannier orbitals is that they are molecular orbitals. Since the new Wannier centers are at Wyckoff position 1*a*, they form a triangular lattice.

We now describe the construction of the Wannier orbitals. Because the system has  $U(1)$  spin rotational symmetry, it is easier to focus on a single spin species to optimize the wave

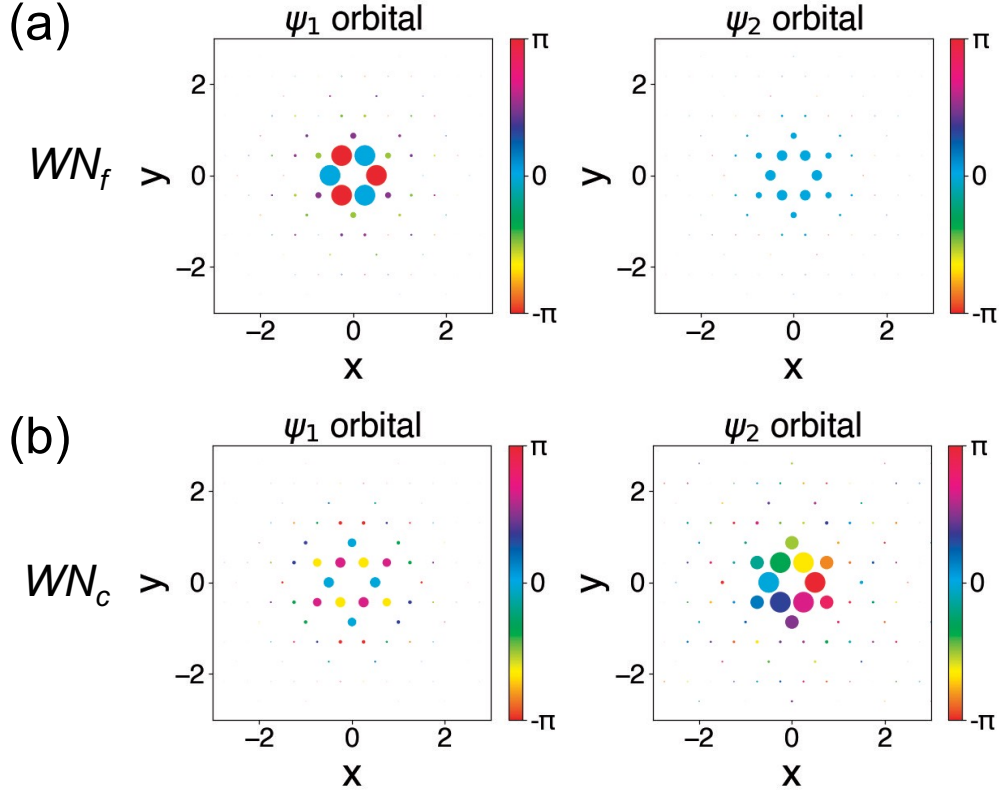


Figure S2: **Emergent Wannier orbitals.** The shape of the Wannier orbital of the spin- $\uparrow$  sector for **a**,  $WN_f$  and **b**,  $WN_c$  in real space. The size (color) of the dot represents the density (phase) of the Wannier function in the  $\psi_1$  and  $\psi_2$  components.

function. The Wannier function for the other spin component can be directly obtained by a Hermitian conjugate. In the following, we focus on the spin- $\uparrow$  sector. We first introduce two trial wavefunctions and use the projection method to determine the Wannier orbitals with the middle two bands. Based on the obtained Wannier functions, we use the Wannier90 software [42] to further optimize them by minimizing the localization functional as defined in Ref. [59]. The initial trial wavefunctions follow the symmetries as deduced above. In other words, for the trial

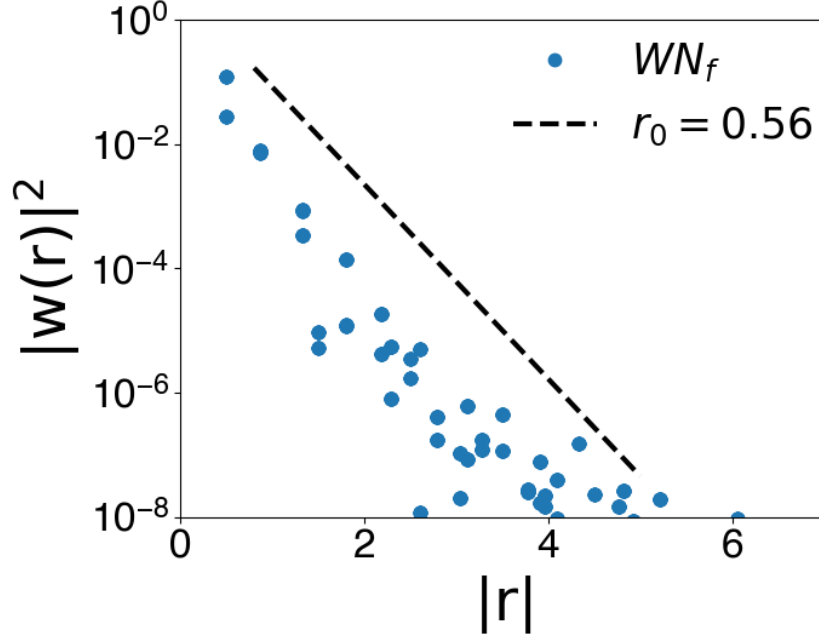


Figure S3: **Decaying of the Wannier function density.** The Wannier functions of the  $f$  electron decay exponentially versus distance.

wavefunctions

$$\begin{aligned}
 |\text{Trial}; f, \mathbf{R}\rangle &= \sum_{\mathbf{r}, i} e^{-|\mathbf{r}-\mathbf{R}|/r_0} w_i^f \psi_{\mathbf{r}, i}^\dagger |0\rangle, \\
 |\text{Trial}; c, \mathbf{R}\rangle &= \sum_{\mathbf{r}, i} e^{-|\mathbf{r}-\mathbf{R}|/r_0} w_i^c \psi_{\mathbf{r}, i}^\dagger |0\rangle
 \end{aligned} \tag{S1}$$

the phase factors  $w_i^f$  and  $w_i^c$  follow the symmetry properties of the single spin sector. The obtained Wannier orbitals are shown in Fig. S2(a,b), in which the components in the original  $\psi_1$  and  $\psi_2$  orbitals are separated into two panels. The size (color) of the dot represents the density (phase) of the Wannier function. As shown in Fig. S3, the obtained Wannier function is exponentially localized. By fitting the envelope of the Wannier function density with  $|w(r)|^2 \sim Ae^{-2r/r_0}$ , we obtain the decaying length scale for the  $WN_f$  to be  $r_0 = 0.56$ . The corresponding decaying length scale for the more extended Wannier function,  $WN_c$ , is somewhat larger,  $r_0 = 0.9$ . The band structure using the new tight-binding parameters in the Wannier basis is plotted in Fig. 2(c). One can easily observe that most parts of the flat band are dominated by the Wannier

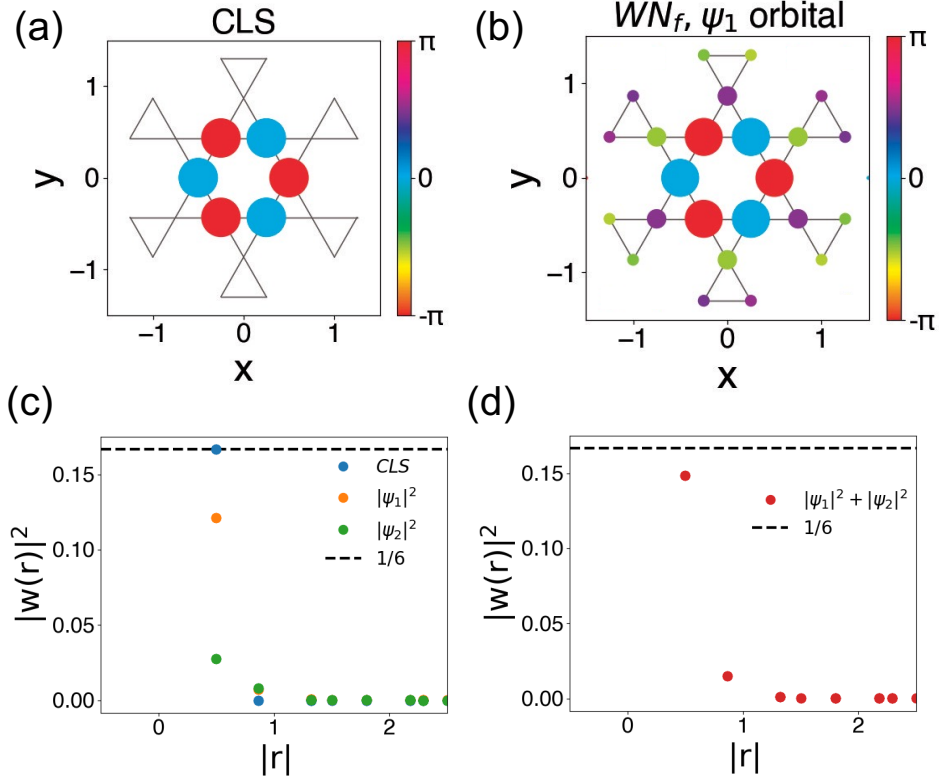


Figure S4: **Comparison between  $WN_f$  and the compact localized state.** Real space representation of **a**, the compact localized state (CLS) and **b**, the tight Wannier function  $WN_f$  projected on to the  $\psi_1$  orbital. Here, size (color) of the dot represents the square root of the density (phase). They share the same phases for the six sites on the middle hexagon, which means they transform the same way under symmetry. **c**, Decaying of the Wannier function density for the compact localized state and the  $WN_f$  in different components, and **d**, the total Wannier function density of  $WN_f$  versus distance. The density of the compact localized state is confined to the middle hexagon. The density of  $WN_f$  has an exponentially decaying tail.

orbital  $WN_f$ .

### C. Relation between $WN_f$ and the compact localized state

The compact localized state, illustrated in Fig. 1(b) and Fig. S4(a), can be derived from the non-interacting Hamiltonian with nearest-neighbor hoppings on a kagome lattice without spin-orbit coupling [32]. The compact localized state centered on a particular hexagon exhibits

nonzero amplitudes on only the six sites of the hexagon [See Fig. S4(a,c)]. While the compact localized states are exact eigenstates making up the flat band, they are not orthogonal, and, more importantly, they do not constitute a complete basis for the flat band since they are not linearly independent [32]. In contrast, the Wannier orbitals,  $WN_f$ , despite sharing the same point group symmetry and center as the compact localized state (see Fig. S4(a,b)), are both orthogonal (see below) and linearly independent, thus forming a complete basis. Furthermore, as depicted in Fig. S4(d), the Wannier function density ( $|w(r)|^2$ ) of the  $WN_f$  are predominantly localized within a single hexagon as well. Although the Wannier orbitals mostly comprise the states from the flat band, they also have weight on the dispersive band near  $\Gamma$  (see Fig. 2(c)), as required by the topological obstruction. The orthogonality of the  $WN_f$  is assured by the Wannierization procedure. This is to be contrasted with the compact localized states, which are not orthogonal: For example, the overlap between two nearest neighbor compact localized states is  $-\frac{1}{6}$ .

To explicitly illustrate this point, we evaluate the overlap between two nearest neighbor  $WN_f$  states. We consider the unit cells centered at an origin,  $\mathbf{R}_0 = \mathbf{0}$  and at  $\mathbf{R}_1 = \mathbf{a}_1 + \mathbf{a}_2$ ; in other words, one anchored by a hexagon and the other centered at the hexagon to its immediate right. The overlap between the  $WN_f$  states associated with these unit cells is specified by

$$\mathcal{O} = \sum_{\text{sites}, \alpha\beta} \mathcal{O}^{\alpha\beta}(x, y), \quad (\text{S2})$$

$$\mathcal{O}^{\alpha\beta}(x, y) = [WN_f(\mathbf{R}_0)]_{\alpha,(x,y)}^* [WN_f(\mathbf{R}_1)]_{\beta,(x,y)},$$

where  $WN_f(\mathbf{R})$  indicates the Wannier function  $WN_f$  centered at  $\mathbf{R}$  and the subscripts “ $\alpha, (x, y)$ ” indicate its components on the orbital  $\psi_\alpha$  at the kagome site  $(x, y)$  in Cartesian coordinates. Note that  $\mathcal{O}^{\alpha\beta}$  is only non-zero when  $\alpha = \beta$ , due to the orthogonality of the two orbitals  $\psi_1$  and  $\psi_2$ . The specific values of the overlap functional,  $\mathcal{O}^{\alpha\alpha}(x, y)$ , are displayed in Table 3, and the corresponding real space representation is depicted in Fig. S5. Table 3 also shows  $\mathcal{O}^{\alpha\alpha} = \sum_{\text{sites}} \mathcal{O}^{\alpha\alpha}(x, y)$ . The sum  $\mathcal{O}^{11} \approx -0.1$ ; the magnitude is of the same order as the overlap between two nearest neighbor compact localized states ( $-1/6$ ). However, in  $WN_f$ ,



$\mathcal{O}^{22}$  is equal to  $-\mathcal{O}^{11}$  (see Table 3). The contributions from the two orbitals exactly cancel out, leading to the overall overlap  $\mathcal{O} = 0$ , i.e. the orthogonality between the  $WN_f$  states.

These observations emphasize the connection between the Wannier orbital  $WN_f$  and the compact localized state. More importantly, they highlight the distinction between the two states.

$(x, y)$	$(\frac{1}{2}, 0)$	$(\frac{1}{4}, \frac{\sqrt{3}}{4})$	$(\frac{1}{4}, -\frac{\sqrt{3}}{4})$	$(\frac{3}{4}, \frac{\sqrt{3}}{4})$
$\mathcal{O}^{11}(x, y)$	-0.1211	$0.0293e^{-i\pi/2}$	$0.0293e^{i\pi/2}$	$0.0293e^{-i\pi/2}$
$\mathcal{O}^{22}(x, y)$	0.02757	0.014734	0.014734	0.014734
$(x, y)$	$(\frac{3}{4}, -\frac{\sqrt{3}}{4})$	$(-\frac{1}{4}, \frac{\sqrt{3}}{4})$	$(\frac{5}{4}, -\frac{\sqrt{3}}{4})$	$(\frac{1}{4}, \frac{\sqrt{3}}{4})$
$\mathcal{O}^{11}(x, y)$	$0.0293e^{i\pi/2}$	$0.01e^{-i0.471\pi}$	$0.01e^{i0.471\pi}$	$0.01e^{-i0.471\pi}$
$\mathcal{O}^{22}(x, y)$	0.014734	$0.00307e^{i0.0477\pi}$	$0.00307e^{-i0.0477\pi}$	$0.00307e^{i0.0477\pi}$
$(x, y)$	$(\frac{1}{4}, -\frac{\sqrt{3}}{4})$	$(1, \frac{\sqrt{3}}{2})$	$(0, -\frac{\sqrt{3}}{2})$	$(0, \frac{\sqrt{3}}{2})$
$\mathcal{O}^{11}(x, y)$	$0.01e^{i0.471\pi}$	$0.0025e^{-i0.003\pi}$	$0.0025e^{i0.003\pi}$	$0.0025e^{-i0.003\pi}$
$\mathcal{O}^{22}(x, y)$	$0.00307e^{-i0.0477\pi}$	$0.00164e^{-i0.047\pi}$	$0.00164e^{i0.047\pi}$	$0.00164e^{-i0.047\pi}$
$(x, y)$	$(1, -\frac{\sqrt{3}}{2})$	$(-\frac{1}{2}, 0)$	$(\frac{3}{2}, 0)$	
$\mathcal{O}^{11}(x, y)$	$0.0025e^{i0.003\pi}$	-0.0008	-0.0008	
$\mathcal{O}^{22}(x, y)$	$0.00164e^{i0.047\pi}$	-0.0005	-0.0005	
$\sum_{\text{sites}} \mathcal{O}^{11}$	$\sum_{\text{sites}} \mathcal{O}^{22}$	$\sum_{\text{sites}} (\mathcal{O}^{11} + \mathcal{O}^{22})$		
-0.10287	0.10287	0		

Table 3: Parts of the overlapping functional  $\mathcal{O}^{\alpha\alpha}$  for two nearest neighbor  $WN_f$ 's on the kagome sites  $(x, y)$ . The sum over all the kagome sites equal to 0, which means the Wannier orbitals are orthogonal to each other. A graphical representation of the same distribution is provided in Fig. S5.

## D. Effective Anderson lattice model

Upon performing the Wannier construction, we can project the original Hamiltonian, defined on the kagome lattice, onto the newly constructed basis to obtain an effective extended Anderson model. The effective Hamiltonian retains all the symmetries from SG191. The specific form of the kinetic part is described by Eq. (6) in the Method section with the parameters listed in Table 4. The hybridization between the Wannier functions  $WN_c$  and  $WN_f$  is offsite, since these

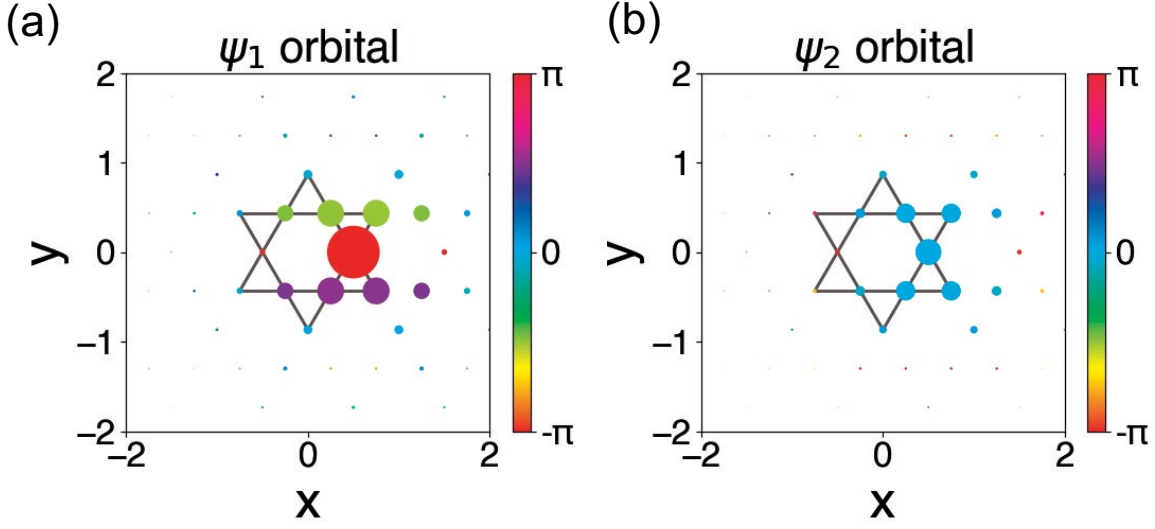


Figure S5: Real space representation of the overlapping functional  $\mathcal{O}^{\alpha\alpha}(x, y)$  in **a**, orbital  $\psi_1$  and **b**, orbital  $\psi_2$ , for two nearest neighbor  $WN_f$ 's at the unit cell  $\mathbf{R}_0 = \mathbf{0}$  and  $\mathbf{R}_1 = \mathbf{a}_1 + \mathbf{a}_2$  as indicated above in Eq. S2 . Here the axis  $x$  and  $y$  label the positions of the kagome sites in the Cartesian coordinate.

two Wannier functions belong to different irreps.

We further project the local Hubbard interaction onto the newly developed Wannier basis, which decays exponentially. It takes the form:

$$\begin{aligned}
H_{int} &= H_{int}^0 + H_{int}^1 + \dots \\
&= \sum_i \left[ u_0^f n_{f\uparrow}^i n_{f\downarrow}^i + u_0^c n_{c\uparrow}^i n_{c\downarrow}^i + F_0 (n_{f\uparrow}^i n_{c\downarrow}^i + n_{f\downarrow}^i n_{c\uparrow}^i) \right. \\
&\quad \left. + (F_0 - J_H^0) (n_{f\uparrow}^i n_{c\uparrow}^i + n_{f\downarrow}^i n_{c\downarrow}^i) + J_H^0 (f_{i\uparrow}^\dagger f_{i\downarrow}^\dagger c_{i\downarrow} c_{i\uparrow} + h.c.) \right] \quad (S3) \\
&\quad + \sum_{\langle ij \rangle} \left[ u_1^f n_f^i n_f^j - 4J_{H_1}^f \mathbf{S}_f^i \mathbf{S}_f^j + u_1^c n_c^i n_c^j - 4J_{H_1}^c \mathbf{S}_c^i \mathbf{S}_c^j \right. \\
&\quad \left. + u_1^{fc} n_f^i n_c^j - 4J_{H_1}^{fc} \mathbf{S}_f^i \mathbf{S}_c^j + \dots \right] + \dots,
\end{aligned}$$

where  $u_0^f$  ( $u_0^c$ ) is the on-site Hubbard interaction of the  $f$  ( $c$ ) electrons. In addition,  $F_0$  and  $J_H^0$  are the on-site interorbital density-density and Hund's interactions. We focus on the case with the  $WN_f$  orbitals near half-filling, for which the  $f$ - $c$  density-density interaction  $F_0$  is

unimportant [36].  $n_\tau^i = n_{\tau\uparrow} + n_{\tau\downarrow}$  and  $\mathbf{S}_\tau^i = \psi_\tau^\dagger \frac{\boldsymbol{\sigma}}{2} \psi_\tau$ , with  $\tau = f/c$ , are the density and spin for the orbital  $\tau$  at site  $i$ , respectively. And  $u_1^\alpha$  ( $J_{H_1}^\alpha$ ), with  $\alpha = f/c/fc$ , represents the nearest neighbor intra/inter-orbital density-density (Hund's) interactions. The values of the  $u_1^\alpha$  is about 1/6 of the  $u_0^\alpha$ . This is because the Wannier function  $WN_f$  is mostly concentrated on the middle six sites of a hexagon. And for the nearest neighbor two  $WN_f$ , they share one corner of the hexagon, leading to a ratio of 1/6. Notice that the interaction Hamiltonian only has the  $U(1)$  symmetry: The  $S_x^i S_x^i + S_y^i S_y^i$  terms are forbidden by the symmetry of the Wannier function. The values of these parameters are listed in Table 5 in unit of the original  $U$ . The on-site Hubbard interaction on the  $f$  orbital is the largest. While other types of interactions can arise during the projection, their magnitudes are smaller compared to the predominant on-site interactions. As a result, we only consider the on-site interaction of the  $WN_f$  orbital in the subsequent EDMFT calculation.

$(i, j)$	$\pm(1, 0)$	$\pm(0, 1)$	$\pm(1, 1)$	$\pm(2, 0)$	$\pm(0, 2)$	$\pm(2, 2)$
$t_{ia_1+ja_2}^f$	0.14119	0.14119	0.14119	-0.01714	-0.01714	-0.01714
$(i, j)$	$\pm(1, 0)$	$\pm(0, 1)$	$\pm(1, 1)$	$\pm(2, 0)$	$\pm(0, 2)$	$\pm(2, 2)$
$t_{ia_1+ja_2}^c$	-0.35511	-0.35511	-0.35511	0.066	0.066	0.066
$(i, j)$	(1, 0)	(0, -1)	(-1, -1)	(-1, 0)	(0, 1)	(1, 1)
$V_{ia_1+ja_2}^{\uparrow(fc)}$	$0.212e^{i1.03}$	$e^{i\frac{\pi}{3}} V_{a_1}^{\uparrow(fc)}$	$e^{i\frac{2\pi}{3}} V_{a_1}^{\uparrow(fc)}$	$e^{i\pi} V_{a_1}^{\uparrow(fc)}$	$e^{i\frac{4\pi}{3}} V_{a_1}^{\uparrow(fc)}$	$e^{i\frac{5\pi}{3}} V_{a_1}^{\uparrow(fc)}$
$(i, j)$	(1, -1)	(-2, -1)	(-1, -2)	(-1, 1)	(1, 2)	(2, 1)
$V_{ia_1+ja_2}^{\uparrow(fc)}$	$0.02e^{-i1.59}$	$e^{i\frac{\pi}{3}} V_{a_1-a_2}^{\uparrow(fc)}$	$e^{i\frac{2\pi}{3}} V_{a_1-a_2}^{\uparrow(fc)}$	$e^{i\pi} V_{a_1-a_2}^{\uparrow(fc)}$	$e^{i\frac{4\pi}{3}} V_{a_1-a_2}^{\uparrow(fc)}$	$e^{i\frac{5\pi}{3}} V_{a_1-a_2}^{\uparrow(fc)}$
$(i, j)$	(2, 0)	(0, -2)	(-2, -2)	(-2, 0)	(0, 2)	(2, 2)
$V_{ia_1+ja_2}^{\uparrow(fc)}$	$0.03e^{i2.078}$	$e^{i\frac{\pi}{3}} V_{2a_1}^{\uparrow(fc)}$	$e^{i\frac{2\pi}{3}} V_{2a_1}^{\uparrow(fc)}$	$e^{i\pi} V_{2a_1}^{\uparrow(fc)}$	$e^{i\frac{4\pi}{3}} V_{2a_1}^{\uparrow(fc)}$	$e^{i\frac{5\pi}{3}} V_{2a_1}^{\uparrow(fc)}$
	$\epsilon_f$	$\epsilon_c$				
	-0.379	1.421				

Table 4: **Parameters for the noninteracting Hamiltonian in the Wannier basis.** Shown here are the intraorbital hopping parameters for the  $f$  and  $c$  orbitals and the hybridization between the  $f$  and  $c$  orbitals for the spin up component. The three rows of the  $(V^{fc})$  denote the nearest, next nearest and next-next nearest hybridization between the  $f$  and  $c$  electrons, respectively. The parameters in the spin-down component are the Hermitian conjugate of their spin-up counterparts.

$u_0^f$	$u_0^c$	$F_0$	$J_H^0$	$u_1^f$	$J_{H_1}^f$	$u_1^c$	$J_{H_1}^c$	$u_1^{fc}$	$J_{H_1}^{fc}$
0.134	0.088	0.103	0.063	0.023	0.005	0.022	0.006	0.033	0.001

Table 5: **Projected interactions in the Wannier basis.** Shown here are the projected interactions in unit of the Hubbard interaction ( $U$ ) in the original Hamiltonian.

## E. Wannier construction of the three-band model

The dispersive band below the targeted flat band is energetically not too far from the flat band. This band is topologically trivial and can be Wannierized alone. Therefore one can construct a tight binding model based on three effective Wannier orbitals with one heavy orbital ( $WN_f$ ) and two light orbitals ( $WN_{c_1}$  and  $WN_{c_2}$ ). The obtained Wannier orbitals are depicted in Fig. S7, with the fitted band structure shown in Fig. S6. In this three-orbital construction,  $WN_f$  and  $WN_{c_1}$  are similar to those obtained in the two-orbital model, while  $WN_{c_2}$  dominates the dispersive band below the flat band. The hybridization strength between the  $f$  orbital and the two  $c$  orbitals, represented by  $V^{fc_1}$  and  $V^{fc_2}$ , depends on the specific parameters of the original Hamiltonian. In the current parameter setting, the maximum value of  $V^{fc_1}$  is approximately 0.2. This is larger than the maximum value of  $V^{fc_2}$ , which is around 0.1. In the low energy limit, a two-channel Kondo model with unequal Kondo couplings flows to a single-channel Kondo fixed point, which is described by the single-channel Kondo lattice model where the  $f$  electrons hybridize with the dominantly-coupled  $c_1$  orbital. Furthermore, the Kondo-destruction quantum criticality is known to be insensitive to the microscopic structure of the conduction electrons [25]. Therefore we focus on the two orbital model in the subsequent calculations.

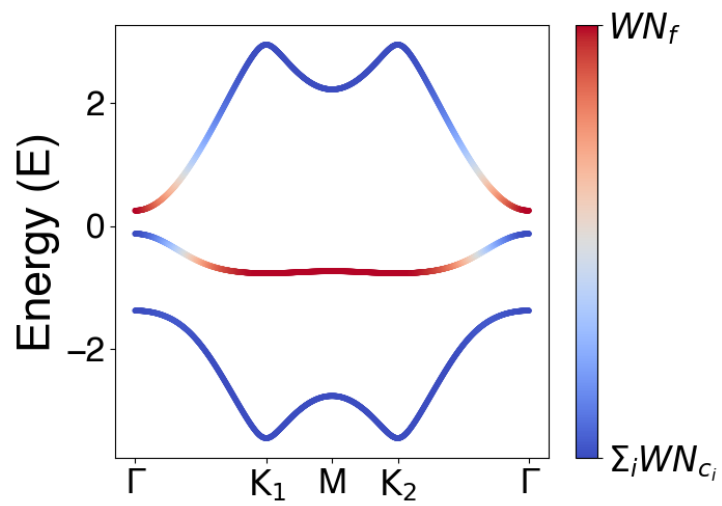


Figure S6: The dispersion of the effective Hamiltonian using three Wannier orbitals, with color indicating the ratio of the orbital components. Here, the summation is over  $i = 1, 2$ , describing the two light Wannier orbitals.

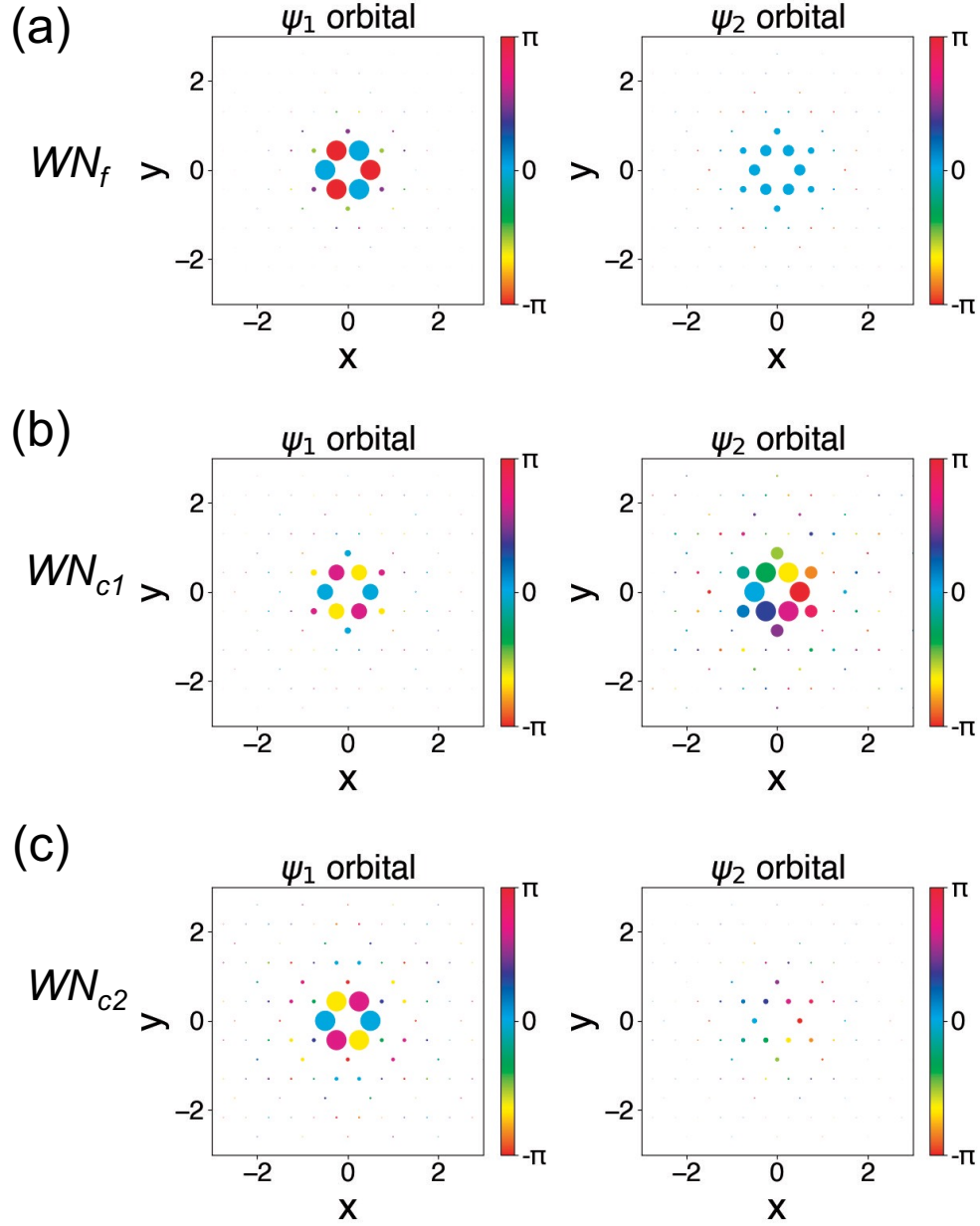


Figure S7: **Emergent Wannier orbitals of the three-band model.** The shape of the Wannier orbital of the spin- $\uparrow$  sector for **a**,  $WN_f$ , **b**,  $WN_{c1}$  and **c**,  $WN_{c2}$  in real space. The size (color) of the dot represents the density (phase) of the Wannier function in the  $\psi_1$  and  $\psi_2$  components.  $WN_f$  and  $WN_{c1}$  are similar to the Wannier construction in the two orbital case, and  $WN_{c2}$  dominates the dispersive band below the flat band.